JACS
JOURNAL OF THE AMERICAN CHEMICAL SOCIETY
pubs.acs.org/JACS
Article

Chloride Reduction of Mn^{3+} in Mild Hydrothermal Synthesis of a Charge Ordered Defect Pyrochlore, $CsMn^{2+}Mn^{3+}F_6$, a Canted Antiferromagnet with a Hard Ferromagnetic Component

Vladislav V. Klepov, Kristen A. Pace, Anna A. Berseneva, Justin B. Felder, Stuart Calder, Gregory Morrison, Qiang Zhang, Melanie J. Kirkham, David S. Parker, and Hans-Conrad zur Loye*

Cite This: J. Am. Chem. Soc. 2021, 143, 11554−11567

ABSTRACT: Geometrically frustrated systems play an important role in studying new physical phenomena and unconventional thermodynamics. Charge ordered defect pyrochlores $AM^{2+}M^{3+}F_6$ offer a convenient platform for probing the interplay between electron distribution over M^{2+} and M^{3+} sites and structural distortions; however, they are limited to compounds with $M^{2+/3+}$ = V, Fe, Ni, and Cu due to difficulties in the simultaneous stabilization of other 3d elements in the +2 and +3 oxidation states. Herein, we employ Cl^- anions under hydrothermal conditions for the mild reduction of Mn_2O_3 in concentrated HF to obtain the $CsMn^{2+}Mn^{3+}F_6$ composition as a phase pure sample and study its properties. The magnetism of $CsMn_2F_6$ was characterized by measuring the magnetic susceptibility and isothermal magnetization data, and a magnetic transition to a canted antiferromagnet state was found at 24.1 K. We determined the magnetic structure of $CsMn_2F_6$ using powder neutron diffraction, which revealed successive long-range ordering of the Mn^{2+} and Mn^{3+} sites that is accompanied by a second transition. The role and strength of magnetic exchange interactions were characterized using DFT calculations.

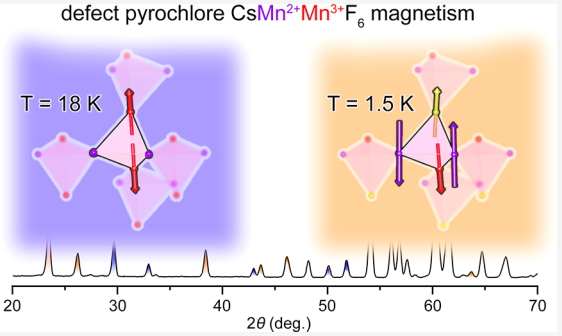

INTRODUCTION

The pyrochlore structure-type has long been used for the design of new materials with a number of potential applications encompassing magnetism,[1−5] oxygen evolution reactions and storage,[6−8] energy storage materials,[9,10] optical materials,[11] and others.[12] The pyrochlore structure, $A_2B_2O_7$, consists of two interpenetrating vertex-sharing tetrahedral frameworks with A and B metal cations, which offers a unique atomic arrangement that promotes frustrated magnetism.[3,13−16] This arrangement has resulted in the development of a number of rare-earth titanate and zirconate compounds exhibiting spin ice and spin liquid behavior.[17−20] A spin ice does not have a single ground state with a minimum energy; on the contrary, magnetic frustration results in multiple ground states with a nonzero residual entropy, making a spin ice material closely related to water ice and offering a unique magnetic system to study quantum effects and abnormal thermodynamics in extended solids. To express the degree of frustration in a material and show how the magnetic ordering temperature deviates from the magnetic exchange interactions, one can use the frustration index $f = |\Theta_{CW}|/T_C$, where Θ_{CW} is the Curie−Weiss temperature and T_C is magnetic ordering temperature. Large values of the frustration index, f, indicate possible candidates for spin liquid materials, and many highly frustrated materials based on pyrochlore structure have been reported to date.

Although the parent pyrochlore structure type is based on an oxide material, other classes of inorganic materials can readily adopt the same structure type, paving a path toward the design of new geometrically frustrated materials. One of the recent advances in this direction has been oxygen replacement with fluorine to create a new class of frustrated materials based on 3d metals with a $NaAB_2F_7$ (A = Ca or Sr; B = Fe, Co, and Ni) composition, which have been grown as large single crystals via the floating zone method.[21−24] Geometric frustration in these pyrochlore antiferromagnets with magnetically coupled 3d cations that occupy one of the two tetrahedrally connected sublattices results in a low temperature spin freezing point and high frustration indexes f, from 19 to 58. Another intriguing class of geometrically frustrated fluorides with composition $AM^{2+}M^{3+}F_6$ (A = alkali cations and NH_4^+, M^{2+} and M^{3+} are 3d transition metal cations such as $Mn^{2+/3+}$, $Fe^{2+/3+}$, Co^{2+}, Ni^{2+}) exhibits a modified pyrochlore structure, in which the A site is half-occupied and one fluorine atom is missing for charge

Received: April 23, 2021
Published: July 26, 2021

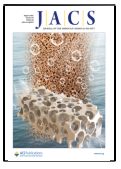

https://doi.org/10.1021/jacs.1c04245
J. Am. Chem. Soc. 2021, 143, 11554−11567

balance.[25,26] $AM^{2+}M^{3+}F_6$ defect pyrochlores can adopt either a disordered cubic structure with both M^{2+} and M^{3+} cations occupying the same site or an orthorhombic structure, in which the 3d metal cations are charge ordered between the two sites. One notable compound that belongs to the cubic crystal systems is $CsNiCrF_6$, which has been extensively studied with respect to its magnetic properties and, despite strong antiferromagnetic interactions between the metal cations, does not exhibit magnetic long-range order at any temperature, with a spin-glass anomaly at about 2.3 K.[27−29] Of all possible M^{2+} and M^{3+} combinations, charge ordered $AM^{2+}M^{3+}F_6$ phases are less numerous and include, for example, $AFe^{2+}Fe^{3+}F_6$ (A = NH_4^+, Rb^+, Cs^+), $AV^{2+}V^{3+}F_6$ (A = Rb^+ and Cs^+), $ANi^{2+}Ni^{3+}F_6$ (A = Rb^+ and Cs^+), $CsCu_2F_6$, $CsAgFeF_6$, NH_4ZnAlF_6, and NH_4CoAlF_6 compositions.[30−39] $RbFe_2F_6$, which has been obtained hydrothermally by reacting respective metal fluorides with trifluoroacetic acid, orders antiferromagnetically at 16 K with two orthogonally oriented magnetic moments on the Fe sites. This compound has a significant frustration index f of 17 and exhibits anharmonic magnon excitations found by neutron spectroscopy.[40] Complete understanding of what drives the formation of charge ordered $AM^{2+}M^{3+}F_6$ orthorhombic phases over the cubic ones is yet to be attained, but some orthorhombic phases, e.g., $CsFe_2F_6$ and CsV_2F_6, undergo a phase transition to the cubic phase upon heating, indicating possible transitions between the two structure types. Since almost all charge ordered defect pyrochlores contain the same 3d element on the M sites, there are still gaps in this family of highly frustrated defect pyrochlores. One group includes the compositions containing Mn on both M sites and has a reverse, as compared to AFe_2F_6, spin arrangement on the M^{2+} and M^{3+} sites, S = 5/2 and 2, respectively, for the Mn compound. Given the overall tetrahedral framework arrangement of the M sites in the AM_2F_6 structure, one would not expect a significant difference in the magnetism upon replacement of Fe by Mn; however, there are distortions in the M coordination environments that can cause a difference in their properties. The purpose of this work was to study the effect of such Fe to Mn replacement and to probe its influence on the properties of the resulting compound belonging to the charge ordered defect pyrochlore family.

In this paper, we report for the first time the hydrothermal synthesis of $CsMn_2F_6$ by Mn_2O_3 reduction with Cl^- and its full magnetic and structural characterization with respect to its nuclear and magnetic structures (Figure 1). We examined the influence of ionic radii of the constituent elements in the structures of 12 $NaAB_2F_7$ and 90 $AM^{2+}M^{3+}F_6$ compounds, revealing that smaller M cations favor the formation of defect pyrochlore structure. The magnetic properties of $CsMn_2F_6$ were characterized by measuring magnetic susceptibility vs temperature and magnetization vs field plots. After finding a magnetic transition at around 24.1 K, we studied the magnetic structure of $CsMn_2F_6$ below this temperature and found a second transition between 10 and 14 K. The magnetic structures support the presence of weak spontaneous magnetization in the sample which stems from its canted antiferromagnetic ordering with a nonzero net magnetization, in contrast to the purely antiferromagnetic $RbFe_2F_6$ analogue. $CsMn_2F_6$ also demonstrates a surprising transition of its ferromagnetic component from an extremely soft, highly susceptible magnet at around 24 K to a hard magnet with coercive field significantly exceeding 5 T at 2 K, suggesting a potential use of such materials for reliable data storage in high magnetic field environments or magnetic field recording.

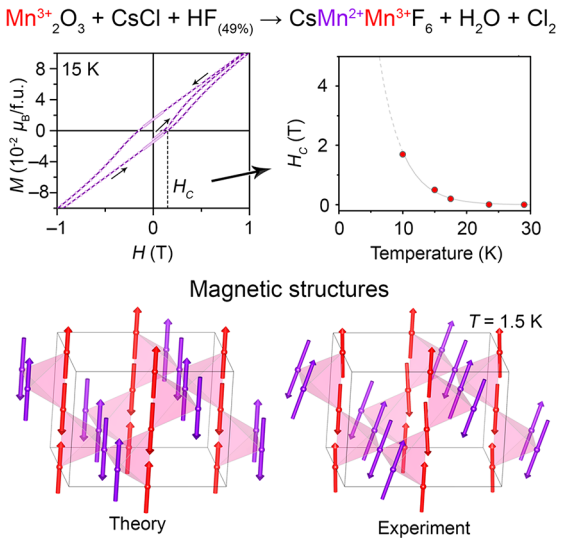

Figure 1. Synthesis of $CsMn^{2+}Mn^{3+}F_6$ via hydrothermal synthesis using CsCl as a reducing agent. $CsMn^{2+}Mn^{3+}F_6$ exhibits a magnetic transition at 24.1 K to a canted antiferromagnetic state, in which (middle) coercive field grows rapidly as temperature decreases (top). The calculated magnetic structure is in a very good agreement with the experimental magnetic structure and highlights the important role of spin canting in its stabilization (bottom).

RESULTS AND DISCUSSION

Synthesis and Crystal Structure. Our successful application of the mild hydrothermal synthesis method has enabled us to prepare a large number of new fluoride compositions, which motivated us to employ this method for obtaining $CsMn_2F_6$.[41−48] After several trial syntheses and reaction conditions optimization, we found that the target phase is formed readily by partial reduction of Mn_2O_3 with CsCl at 200 °C ($E^0(Mn^{3+}/Mn^{2+})$ = 1.54 V, $E^0(Cl_2/2Cl^-)$ = 1.36 V) in concentrated HF according to the following equation

$$2Mn_2O_3 + 2CsCl + 12HF = 2CsMn^{2+}Mn^{3+}F_6 + 6H_2O + Cl_2$$

We found that the product of the reaction is strongly dependent on the Mn_2O_3 to CsCl ratio. A phase pure sample of $CsMn_2F_6$ can be obtained using a 1:2 ratio, while even a slight deviation from this ratio or from the quantity of HF used results in the formation of side products, e.g., $CsMnF_4{\cdot}2H_2O$, $CsMnF_4$, $CsMnCl_3{\cdot}2H_2O$, or MnF_2.[49] To illustrate the role of the chloride ion as a reducing agent, we performed a series of reactions where CsCl was gradually replaced by CsF. Upon decreasing of the CsCl content in the reaction, the amount of Mn^{3+}-containing side products, $CsMnF_4{\cdot}2H_2O$ and $CsMnF_4$, increases (Figures 2 and S1, Table S1). Ultimately, a complete substitution of CsCl by CsF results in the formation of only Mn^{3+}-containing products $CsMnF_4$ and $CsMnF_4{\cdot}2H_2O$. At the same time, additional sources of Cl^- (e.g., HCl) in the reaction lead to the formation of Mn^{2+}-containing products, such as $CsMnCl_3{\cdot}2H_2O$ and MnF_2.

Although a number of related fluorides with formula $AM^{2+}M^{3+}F_6$ were obtained using flux methods and large (mm^3 to cm^3 size scale) single crystals were grown,[25] our own attempts to grow large crystals of $CsMn_2F_6$ using fluxes were

https://doi.org/10.1021/jacs.1c04245
J. Am. Chem. Soc. 2021, 143, 11554−11567

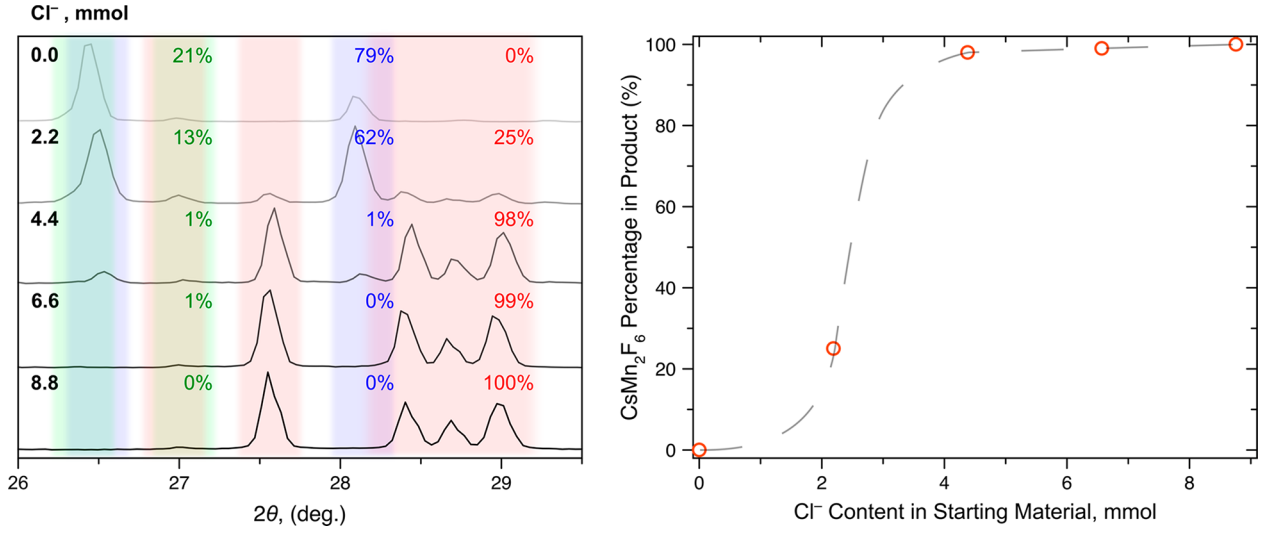

Figure 2. PXRD of the product for the reaction between Mn_2O_3, CsCl, and CsF as a function of the CsCl/CsF molar ratio in 2θ range 26.0−29.5 deg (left). Red, blue, and green areas highlight the diffraction peaks for $CsMn^{2+}Mn^{3+}F_6$, $CsMn^{3+}F_4$, and $CsMn^{3+}F_4{\cdot}2H_2O$, respectively. Red, blue, and green percentages are the content of $CsMn^{2+}Mn^{3+}F_6$, $CsMn^{3+}F_4$, and $CsMn^{3+}F_4{\cdot}2H_2O$, respectively, estimated using whole pattern fitting. $CsMn_2F_6$ percentage in the product as a function of Cl^- content in the starting reaction mixture (right).

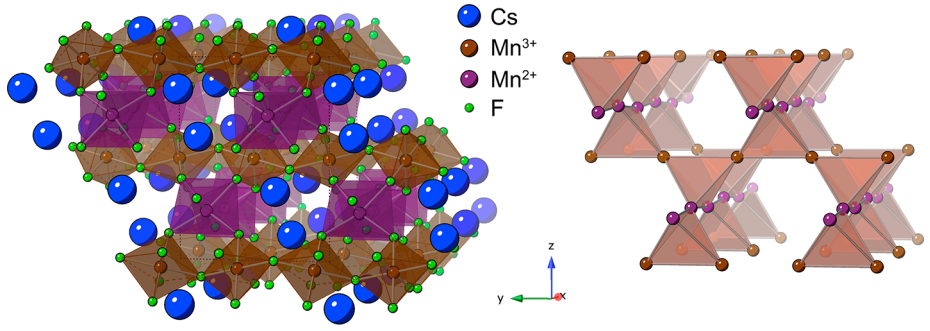

Figure 3. A view down the *x*-axis of the structure of $CsMn_2F_6 \equiv CsMn^{2+}Mn^{3+}F_6$ (left) and its Mn-sublattice, which consists of corner sharing $Mn^{2+}{}_2Mn^{3+}{}_2$ tetrahedral units (right).

not successful and resulted in the formation of known manganese fluorides. Larger single crystals (~0.1 mm^3) were grown via partial replacement of CsCl with CsF and use of more diluted HF, creating less reducing conditions and slowing down the crystallization process. The purity of the product was confirmed by powder X-ray diffraction (PXRD) and neutron diffraction; moreover, no magnetic transitions that can be associated with other manganese phases were found in the magnetic susceptibility data.

We determined the structure of $CsMn_2F_6$ using single crystal X-ray diffraction and found that it crystallizes in a distorted defect pyrochlore structure (*Pnma* space group, Tables S2 and S3) with unit cell parameters a = 7.3013(2) Å, b = 7.7141(2) Å, and c = 10.1926(3) Å. The unit cell parameters agree well with previously reported values found from PXRD data, but the crystal structure of this compound has not been reported.[50] The structure consists of distorted MnF_6 octahedra that are connected through the vertices to build up a framework with pores that are occupied by Cs cations (Figure 3). The Mn−F bond distances allow for unambiguous distinction between the Mn^{2+} and Mn^{3+} cations: the $Mn^{2+}F_6$ octahedra have four longer, 2.1535(12)−2.1612(13) Å, and two shorter, 2.0205(18) and 2.0416(18) Å, bonds, while $Mn^{3+}F_6$ octahedra exhibit four shorter, 1.8594(12)−1.8682(12) Å, and two longer, 2.0414(6) Å, bonds (Table S4). The bond-valence sum calculations result in values of 1.97 and 3.02 for Mn^{2+} and Mn^{3+}, respectively, indicating a fully charge ordered distribution of the Mn atoms in the structure. In contrast to the $RbFe^{2+}Fe^{3+}F_6$ analog, in which Fe^{3+} atoms are located in a nearly regular octahedral environment with Fe^{3+}−F distances varying over the range of 1.91−1.95 Å, the geometry of the $Mn^{3+}F_6$ octahedron is strongly affected by a Jahn−Teller distortion.[50] Interestingly, although the other Mn site should not be affected by a Jahn−Teller distortion, as it contains a $3d^5$ cation, there is nonetheless a strong distortion of the $Mn^{2+}F_6$ octahedron, in which one of the F−Mn−F angles is 111.15(7)° (Table S5), which can be attributed to either a structural distortion inherent to the structure type or to a cooperative Jahn−Teller distortion.[38] In the Mn sublattice, each Mn is separated from six other surrounding Mn by 3.63−3.86 Å, creating a nearly uniformly spaced net of magnetically interacting Mn atoms.

As the structure is influenced by the size of its constituent elements, we made an attempt to identify the size parameters that favor the formation of defect pyrochlores as well as their preference for either the ordered or the disordered structure type. Lui and co-workers introduced a tolerance factor for the pyrochlore structure type based on $A_2M_2O_7$ series and defined it as $\tau = \frac{3(R(A)+R(O))}{\sqrt{17}((R(M)+R(O)))}$, where τ falls into a small range of

https://doi.org/10.1021/jacs.1c04245
J. Am. Chem. Soc. 2021, 143, 11554−11567

0.826−0.943 for pyrochlore oxides.[51] By using the same equation for over 90 defect pyrochlore fluoride structures of the type $AM^{2+}M^{3+}F_6$, we found that all of them have a tolerance factor ranging from 1.032 to 1.191 (Table S9), whereas for 12 pyrochlore fluorides of the type $A\acute{A}M^{2+}{}_2F_7$, the tolerance factor ranges between 0.925 and 0.974 (Table S10). Given that there is a gap between the two ranges for fluoride structures, one can surmise that a regular pyrochlore structure will likely form for $\tau < 1$, whereas a $\tau > 1$ indicates a higher probability of defect pyrochlore formation. We found it less straightforward to predict which variation of the defect pyrochlore structure, ordered orthorhombic or disordered cubic, will form based on the size of the constituent ions. Since a larger difference between M^{2+} and M^{3+} ionic radii should promote the formation of the charge ordered phase as the large size difference hinders two elements from sharing the same site,[39] we plotted the size difference as a function of the A cation ionic radius (Figure 4). Although a large M cation size

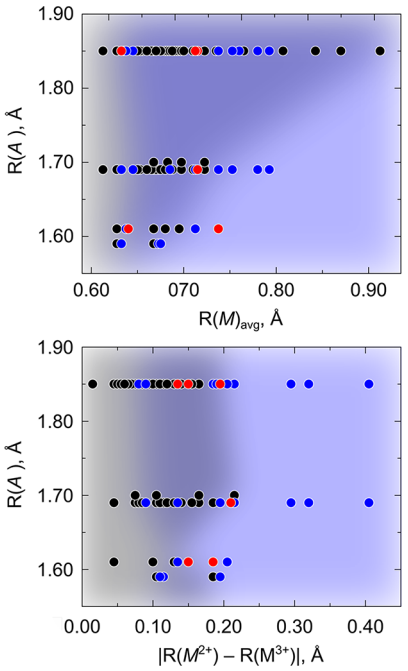

Figure 4. Radius of the A cation (top) vs the size difference between M^{2+} and M^{3+} cations and (bottom) average B site size in the $AM^{2+}M^{3+}F_6$ defect pyrochlore family. Black and blue circles correspond to disordered cubic and charge ordered orthorhombic pyrochlores, respectively. Compounds that crystallize in both charge ordered and disordered structures or exhibit a high temperature transition from orthorhombic to cubic phase are shown with red circles. Gray and blue areas schematically represent the stability range for the cubic and orthorhombic pyrochlore phases, respectively. Ionic radii data were taken from Shannon[52] and NH_4^+ ionic radii data were taken from ref[53] where for A and M cations coordination numbers of XI and VI were used, respectively.

difference, > 0.25 Å, clearly favors the formation of the ordered structure, both structure types are observed when the size difference falls below 0.25 Å. Molokeev et al. showed that another possible reason for symmetry lowering from cubic to orthorhombic is a mismatch between the A- and average M-site sizes, in which a small A cation size can cause a structural distortion that reduces the volume that the A cation occupies.[34] As can be seen from Figure 4, there is a large number of cubic phases with $A = Cs^+$ or Rb^+ when the average size of the framework-forming M cations is below 0.72 Å. For even smaller A-cations ($A = NH_4^+$ and K^+) both the cubic and the orthorhombic phases form for an average M-site size range of 0.60−0.70 Å. The importance of the A-site cation size can also be illustrated by an orthorhombic to cubic phase transition at high temperatures observed in several orthorhombic AM_2F_6 phases. Although one would expect all thermal motion in an AM_2F_6 structure to change simultaneously with the temperature, neutron diffraction studies on $RbFe^{2+}Fe^{3+}F_6$ have revealed that the thermal ellipsoids, and thus the effective radius, of the A-site cation increases disproportionally faster than the other sites in the structure as the temperature increases, reducing the size difference between the A- and M-sites.[33] Due to this, compositions such as RbV_2F_6, CsV_2F_6, and $CsFe_2F_6$ adopt a charge ordered orthorhombic structure type at room temperature and undergo a transition to the cubic structure type, accompanied by charge disordering, at high temperature.

A reversible transition from orthorhombic to cubic defect pyrochlore is facilitated for compositions where both M^{2+} and M^{3+} sites are occupied by the same element in the +2 and +3 oxidation states, resulting in an abundance of orthorhombic phases with ternary vs quaternary compositions. In fact, all ternary AM_2F_6 defect pyrochlores are orthorhombic because, for them, the cubic to orthorhombic transition can readily be achieved by a simple charge (i.e., electron) redistribution. In contrast, the transition from cubic to orthorhombic in quaternary $AM^{2+}\acute{M}^{3+}F_6$ phases has to be accompanied by the redistribution of the actual cations. For that reason, the disordered cubic phase can be obtained under either high temperature conditions in flux reactions with $T > 1000$ °C,[25] where the effective size of the A cations is high due to disproportionally high increase in their thermal motion in the resulting crystal structure, or by entangling the mobility of the M cations (Figure 5). A good illustration of the latter is the recently obtained $(NH_4)MnFeF_6$ defected pyrochlore, which can be synthesized as a cubic phase via ball milling of the

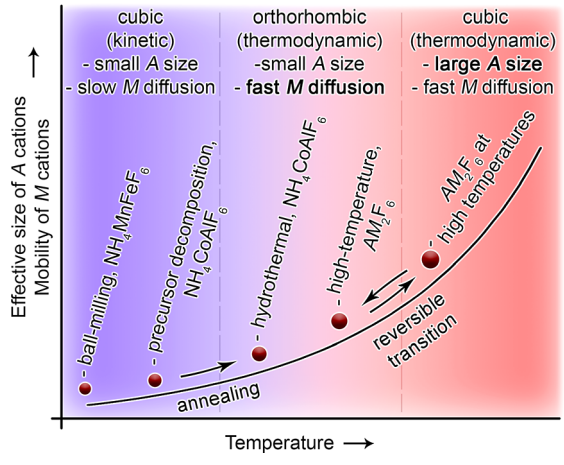

Figure 5. A schematic representation of defect pyrochlore structure stability as a function of temperature. Low diffusion rates at low temperature stabilize the cubic phases with M^{2+} and M^{3+} statistically distributed over the M site. Intermediate temperature range with fast M cation diffusion promotes the formation of the orthorhombic phases. At high temperatures, the cubic phase is stabilized due to the A cation large effective size, which increases disproportionately relative to the size of other cations.

https://doi.org/10.1021/jacs.1c04245
J. Am. Chem. Soc. 2021, 143, 11554−11567

fluoride precursors.[54] Another example is the decomposition of $[Co^{3+}(NH_3)_6]AlF_6$ at 280 °C, which results in the formation of cubic $NH_4Co^{2+}AlF_6$, whereas a reaction between CoF_2, AlF_3, and NH_4F under hydrothermal conditions at 400 °C yields an ordered orthorhombic phase.[39] Moreover, the cubic phase of NH_4CoAlF_6 can be transformed to the orthorhombic one by annealing it at 350 °C for 1 week, which enables the mobility of the M cations in the solid state, illustrating the metastable nature of the cubic phase. One would expect that the phases in the intermediate size difference regime in Figure 4 could also undergo a similar cubic to orthorhombic ordering transition through prolonged heating at elevated temperatures; although, as of yet, there are no reports in the literature of this process. The overall conclusion is that the formation of the orthorhombic phases is favorable for the ternary phases and can be promoted by 1) a larger difference between the M^{2+} and M^{3+} cation sizes, 2) a smaller size of the A cation, and 3) midtemperature reaction conditions, whereas the formation of the cubic phases is unlikely for the ternary phases and can be promoted by either 1) high temperature flux synthesis or 2) the decomposition of a precursor at rather low, below 300 °C, temperatures.

We performed thermogravimetric analysis of $CsMn_2F_6$ under a nitrogen flow to probe if it undergoes a phase transition to the tetragonal or cubic crystal system, as was observed in the case of the $CsFe_2F_6$ analog. The differential thermal analysis (DTA) data showed an endothermal effect with an onset temperature of 410 °C, which is not associated with any weight loss (Figure S2). Such an effect could be indicative of a phase transition and high temperature PXRD (HT PXRD) was employed to check this possibility. PXRD patterns of a powder sample of $CsMn_2F_6$ were collected under a vacuum up to 500 °C with 50 °C step intervals (Figure S3). The PXRD patterns from room temperature to 400 °C indicate no changes in the sample symmetry, followed by sample decomposition at a temperature between 400 and 450 °C, in a good agreement with the DTA endothermic peak observed at 410 °C. As the decomposition products could not be identified from the HT PXRD pattern, a fresh sample of $CsMn_2F_6$, which was placed into a carbon crucible and sealed under a vacuum inside a silica tube, was heated to 450 °C overnight and an ex-situ room temperature PXRD pattern was collected. In the silica tube reaction, two major products formed during the decomposition, MnF_2 and Cs_2MnF_6, along with a Mn_2O_3 impurity due to a reaction between $CsMn_2F_6$ and residual moisture and air in the tube, indicating the disproportionation of Mn^{3+} in the fluoride starting compound. Although MnF_2 and Cs_2MnF_6 do not match with the HT PXRD pattern at 450 °C, both methods confirm the thermal decomposition of $CsMn_2F_6$ at a temperature between 400 and 450 °C and a lack of a structural transition to the tetragonal or cubic crystal system.

Magnetism. The magnetic properties of $CsMn_2F_6$ were characterized by collecting data of DC magnetic susceptibility vs temperature over the 2−300 K range using polycrystalline powder and also a multidomain single crystal (Figures 6 and S4, respectively). The magnetic susceptibility plot can be divided into two temperature regions: a low-temperature region below 100 K in which a magnetic transition is visible at 24.1 K and high-temperature region (100 to 300 K) exhibiting Curie−Weiss behavior. The inverse magnetic susceptibility data were fitted with a linear function over the 150−300 K range (Figure 6), and a Weiss temperature of −93.7 K was

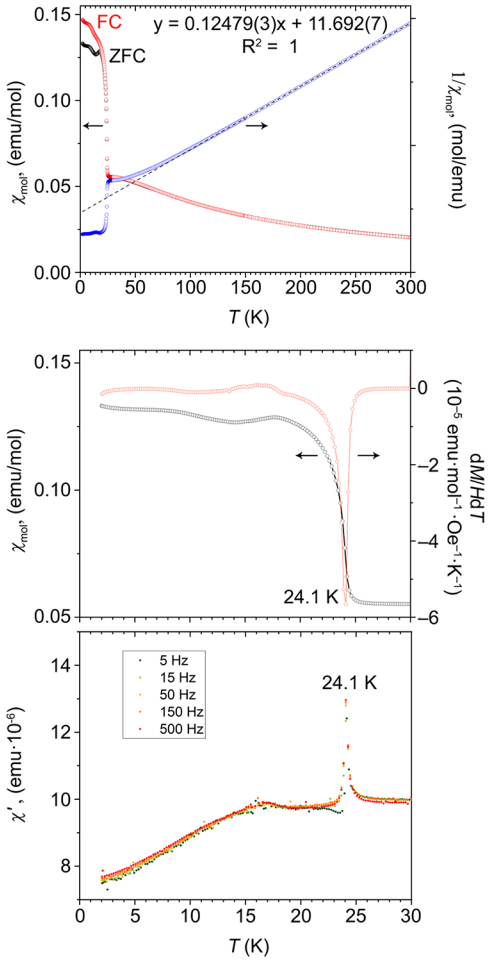

Figure 6. DC molar magnetic susceptibility (χ_{mol}) and inverse susceptibility (χ_{mol}^{-1}) vs temperature plots of polycrystalline $CsMn_2F_6$ (top). Enlarged 0−30 K region showing zero-field cooled χ_{mol} vs T plot along with dM/dHT vs T plot, which exhibits only one peak corresponding to a magnetic transition at 24.1 K (middle) and AC susceptibilities as a function of temperature and frequency (bottom).

derived from it, indicating antiferromagnetic correlations in the sample. Dividing the Weiss temperature by the ordering temperature results in a frustration index f of 3.9, which indicates low frustration in the system. The measured magnetic moment per formula unit of 8.01 μ_B is above the theoretical value of 7.68 μ_B that was calculated using the spin-only magnetic moments for Mn^{2+} and Mn^{3+} cations, 5.92 and 4.90 μ_B, respectively. Although higher experimental magnetic moments for Mn^{3+} have been previously reported and can be one possible explanation of higher than expected paramagnetic moment of $CsMn_2F_6$,[55,56] the moment can also be adjusted to lower values by including a small temperature independent paramagnetic (TIP) component. While fitting the data to a modified Curie−Weiss law results in a negligibly small negative χ_0 ($\chi_0 \sim -0.00009$ emu/mol), using a small positive χ_0 of 0.0011 emu/mol results in a magnetic moment of 7.66 μ_B (Figure S5), which is in good agreement with the expected theoretical value of 7.68 μ_B, and insignificantly decreases the quality of the data fit, see Figure S5. In the low temperature region, below 100 K, the susceptibility plot deviates from Curie−Weiss behavior and ultimately undergoes a transition to an ordered magnetic state. The dM/dHT vs T plot indicates a clear transition at 24.1 K (Figure 6); there are

https://doi.org/10.1021/jacs.1c04245
J. Am. Chem. Soc. 2021, 143, 11554−11567

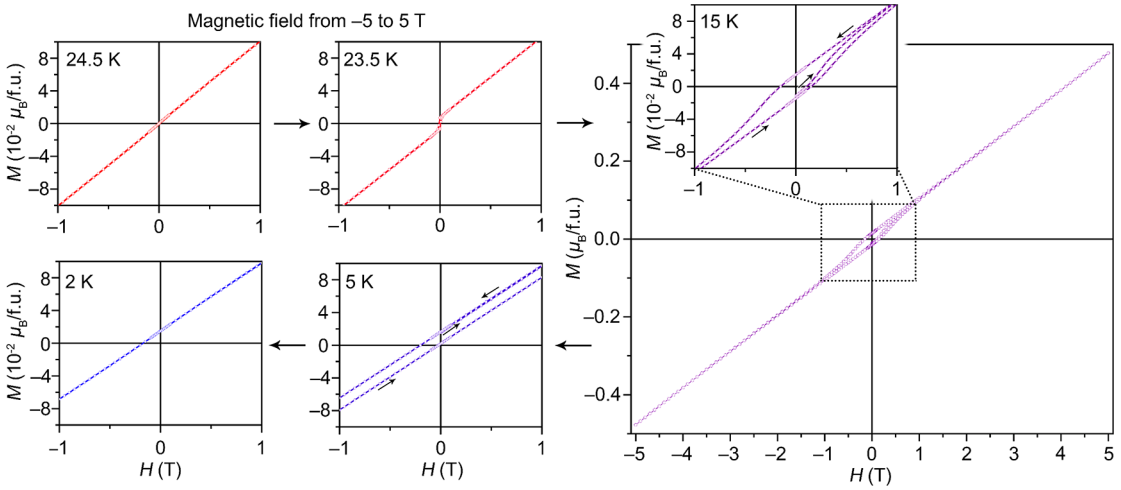

Figure 7. Magnetization as a function of field $M(H)$ plots of $CsMn_2F_6$ measured at 24.5 (above $T_c \approx 24.1$ K), 23.5 (slightly below T_c), 15, 5, and 2 K. All samples were measured with −5 to 5 T field sweeps, but only −1 to 1 T regions are shown. There is a weak metamagnetic transition at 23.5 K corresponding to an easy magnetization reversal when a weak magnetic field is applied. As temperature decreases, the coercive field of the ferromagnetic component increases until it becomes a very hard magnet at 5 K that cannot be fully reversed with a field of 5 T. At 2 K, the sample retains its starting magnetization even when a full 5 to −5 T sweep is made, indicating a very hard ferromagnetic component in the sample. The orientation of initial magnetization depends on the direction of a residual magnetic field in the instrument.

no other apparent transitions at lower temperatures. A small difference in the magnetization between the ordered and paramagnetic states, ∼ 0.012 vs ∼0.005 emu, indicates either a ferri- or canted antiferromagnetic ordering in the sample. The AC data exhibit a single sharp peak at a temperature of 24.1 K, indicating a single transition to a long-range ordered magnetic state. The sample is unlikely to exhibit spin liquid behavior based on the overlapping AC susceptibility plots collected at different frequencies (Figure 6).

To better understand the nature of the low temperature magnetic transition, a series of magnetization vs field (MvH) data were collected in the temperature range of 2 to 25 K. Above 24 K, the MvH plots exhibit a proportional change of the magnetization as a function of field (Figure 7), which is typical for paramagnetic samples that do not reach their saturation magnetization in the applied field. Right below the transition temperature, at 23.5 K, the magnetization changes rapidly when a weak nonzero field is applied in either direction, indicating a weak metamagnetic effect as the applied field H approaches zero. At temperatures between 23.5 and 10 K, a hysteresis loop appears and extends to stronger fields as the temperature decreases. The low remnant magnetization of the sample and its linear behavior in higher applied fields indicates a small ferromagnetic component in a predominately antiferromagnetic system, which is characteristic of ferrimagnets or canted antiferromagnets. It is worth noting that all hysteresis curves start with a nonzero magnetization, despite demagnetization of the sample by warming it to room temperature after each MvH data collection and zero-field cooling to the next measurement temperature. The nonzero magnetization is likely due to the metamagnetic transition at 23.5−24.5 K: when crossing this temperature region, even a small applied field, such as a residual field in a SQUID instrument, can magnetize the sample. Our attempts to minimize the residual field by using scans with the Pd standard were not successful, and even a small, nearly undetectable field well below 10^{-4} T resulted in sample magnetization upon cooling. The MvH plots below 10 K show gradual "closing" of the hysteresis loop until it turns to a direct proportional dependence of the applied field on the magnetization, with an offset magnetization value. It is noteworthy that at even a 5 T applied field does not change the magnetization of the sample and shows that the ferromagnetic component in the sample turns from an extremely soft magnet that is sensitive to the applied field at around 24 K to a very hard one at 2 K.

Since the small ferromagnetic component in the magnetization vs field plots are obscured by a significant antiferromagnetic component, we derived the ferromagnetic components' M vs H plots by subtracting linear antiferromagnetic contributions from the full magnetizations (Figure 8). The derived plots show a clear magnetic transition at 23.5 K with a small saturation moment of 0.8×10^{-2} μ_B/f.u. As the temperature decreases to 20 K, one can observe a hysteresis

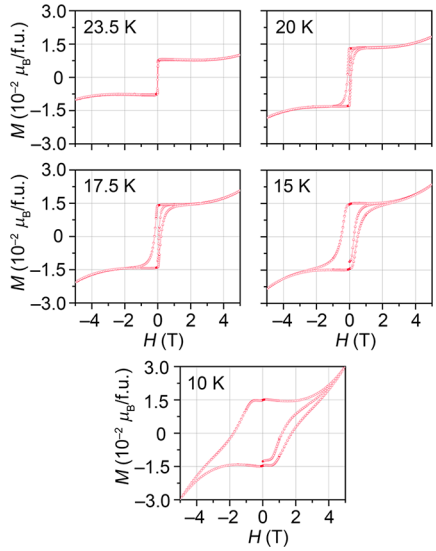

Figure 8. Magnetization as a function of field plots for ferromagnetic components of $CsMn_2F_6$ between 23.5 and 10 K. The plots were derived by fitting linear antiferromagnetic part and subtracting it from the magnetization vs field plots shown in Figure 7.

https://doi.org/10.1021/jacs.1c04245
J. Am. Chem. Soc. 2021, 143, 11554−11567

loop with a coercive field $H_c \approx 0.1$ T, which then nonlinearly increases as temperature decreases, to ≈0.2 and 0.5 T at 17.5 and 15 K, respectively. When the temperature approaches 10 K, H_c reaches a high value of ≈1.7 T. A further temperature decrease hardens the ferromagnetic component, and even a 5 T maximum magnetic field is insufficient to fully revert the magnetization and to establish the coercive field of the sample at 5 and especially 2 K, where no change of remnant magnetization occurs after a full −5 → 5 T field sweep of the sample. The "locked" remnant magnetization suggests that the coercive field in the sample is significantly higher than the maximum applied field, 5 T, and provides evidence of a dramatic change of coercive field in a narrow temperature range, from $H_c \approx 0$ at a transition temperature of 24.1 K to $H_c \gg 5$ T at 2 K. Such an effect, if used in a low temperature environment, such as space, or if brought to a more practical temperature range, can have potential applications in long-term information storage in situations where reliable data preservation is needed when the data storage device is exposed to high magnetic fields. Further characterization of the sample and the understanding of the remnant magnetization origins required magnetic structure characterization of the sample.

Neutron Diffraction and Magnetic Structures. To determine the magnetic structure of $CsMn_2F_6$ and to further characterize the "locked" remnant magnetization effect at low temperatures, we collected temperature dependent neutron diffraction data. Several diffraction peaks appeared below the transition temperature of ∼24.1 K (Figures 9 and S6−S24) that indicate long-range magnetic order and that correspond to a propagation vector $\mathbf{k} = (0,0,0)$. We found a good fit to the experimental data below the transition point by refining the magnetic structure in the *Pnm'a'* magnetic space group. The magnetic structure refinement revealed a large magnetic moment on the Mn^{3+} atoms, 3.25(2) μ_B at 18 K, which aligned in a canted antiferromagnetic fashion with an angle of 167.2° between two neighboring magnetic vectors (Figure 10). The other Mn-sublattice exhibits a low magnetic moment of 0.59(5) μ_B, which is inconsistent with the $3d^5$ configuration of the Mn^{2+} atoms and indicates only a partial magnetic ordering of the sites. Like the Mn^{3+}-sublattice, the magnetic moments on the Mn^{2+} atoms exhibit canted antiferromagnetic ordering. The net magnetic moment of the unit cell, 0.83 μ_B at 18 K, is aligned along the *a* direction, and mostly consists of the magnetic moment on the Mn^{2+} atoms, 0.636 μ_B along the *a* axis (Table S7). The magnetic moments along the other two directions cancel each other out due to symmetry constraints on both Mn sites.

At a temperature of 10 K and below, the magnetic structure refinement resulted in an unaccounted intensity on the magnetic peaks along with the emergence of additional magnetic peaks, indicating that the sample undergoes a second magnetic transition, which was not detected in the magnetic susceptibility data. A search through the subgroups of the *Pnm'a'* group revealed $P2_1/c$ as a potential lower symmetry magnetic space group, which was confirmed by the successful Rietveld refinement of the neutron diffraction data (Figures S22−S24). In the low temperature magnetic structure at 1.5 K, the Mn^{3+} atomic positions, which already acquired a high moment after the first transition, split into two crystallographically independent positions, Mn1_1 and Mn1_2, and slightly increase their magnetic moments from 3.25(2) to 3.40(3) and 3.52(4) μ_B, while the Mn^{2+} cations significantly increase their magnetic moments from 0.59(5) to 4.13(3) μ_B,

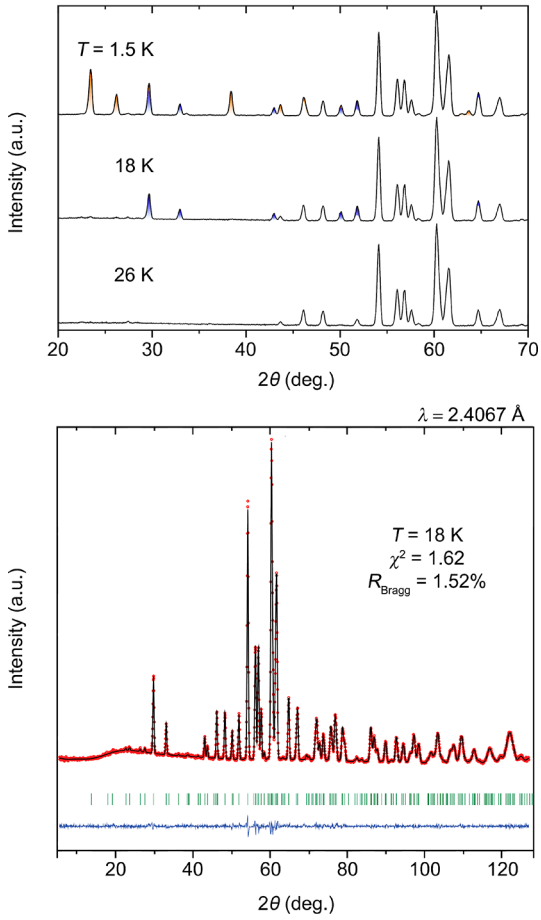

Figure 9. Neutron diffraction patterns of $CsMn_2F_6$ at 26, 18, and 1.5 K (top). The compound undergoes a transition first from the *Pnma* to the *Pnm'a'* magnetic space group and then to the $P2_1/c$ space group. Diffraction peaks due to magnetic ordering are highlighted with blue and orange for the first and the second transition, respectively. Rietveld refinement plot of neutron diffraction data collected at 18 K (bottom).

in perfect agreement with the higher unpaired electron count on the Mn^{2+} cations. The Mn^{2+} sites show significant increase of their magnetic moments along the *b* axis, which are prohibited by symmetry in the *Pnm'a'* space group. The net magnetic moment in the unit cell is symmetry constrained along the *a* axis of the original cell (corresponds to the *b* axis in the standard setting of the $P2_1/c$ space group) and is equal to 0.69 μ_B (Table S8). Unlike in the higher temperature magnetic structure, the net moment is dominated by the contribution from Mn1_1 and Mn1_2 atoms, while the moment on the Mn2 sites is oriented in an antiparallel fashion, reducing the overall magnetic moment of the cell. The small value of the net magnetization, which corresponds to a weak canting of predominantly antiferromagnetically ordered spins and which is almost unchanged during the second phase transition (0.64 vs 0.69 μ_B), agrees well with the absence of any significant changes in the susceptibility data and the presence of the remnant magnetization observed in the sample in *M* vs *H* plots (Figure 7).

Neutron diffraction data that were collected in a temperature range between 1.5 and 24 K allowed us to examine how the magnetic moments on both lattices vary as the temperature changes (Figure 10). The moment on the Mn1 rapidly

https://doi.org/10.1021/jacs.1c04245
J. Am. Chem. Soc. 2021, 143, 11554−11567

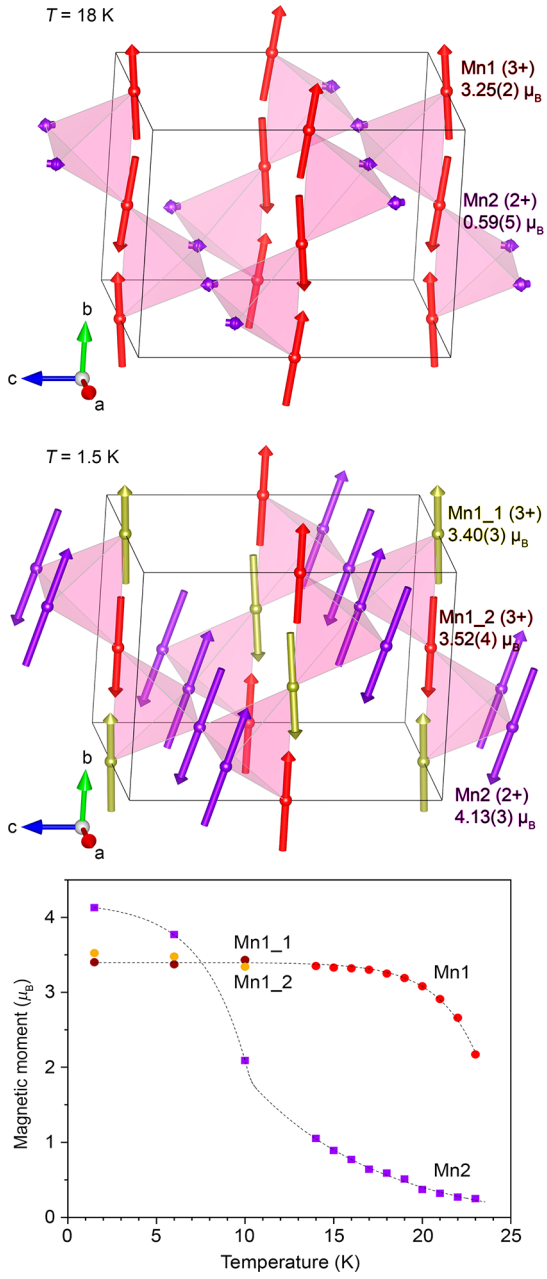

Figure 10. Magnetic structure of $CsMn_2F_6$ at 18 K (top) and 1.5 K (middle). Magnetic moments on the manganese atoms in the magnetic structure of $CsMn_2F_6$ at 1.5, 6, 10, and 14−23 K (bottom). The dashed lines are guides to the eye.

saturates as the temperature decreases, reaching ≈3.3−3.4 μ_B at 17 K. Transition to the low temperature modification splits the site into two, but the magnetic moment on both sites stays at approximately the same saturation value. The magnetic moment on the Mn2 sites displays a different behavior: at first it slowly increases with an increasing rate as the temperature decrease, then rapidly increases at around the second transition temperature, and finally reaches a maximum at 1.5 K. Although there are not enough data points at low temperatures, one can surmise that the moment of 4.13(3) μ_B found for Mn2 site at 1.5 K is very close to its saturation limit.

There are a number of compounds with $AM^{2+}M^{3+}F_6$ composition, but only a few of them exhibit charge ordering and long-range magnetic ordering of the M sites.[33−35,40,57,58] Among them is a series of isostructural iron compounds $AFe^{2+}Fe^{3+}F_6$ (A = NH_4^+, Rb^+, Cs^+) that undergo a one-step antiferromagnetic transition at temperatures of 19, 16, and 13.7 K, respectively.[31,33,34,57] Although only the magnetic structures of the NH_4^+ and Rb^+ analogs have been reported, similar magnetization behavior of $CsFe_2F_6$ suggests that it might have a similar magnetic structure. As in $CsMn_2F_6$, the nuclear and magnetic unit cell in $NH_4Fe_2F_6$ and $RbFe_2F_6$ have identical metrics; however, the symmetry of the $CsMn_2F_6$ magnetic unit cell after the first transition is different from the symmetry of the Fe-based analogs. Both Fe containing compounds undergo a transition to the *Pnma* magnetic space group (#62.441), in which the net unit cell magnetization is constrained to zero by symmetry. The Fe1 sites can have magnetic components in all three M_x, M_y, and M_z directions and the Fe2 site moment is restrained to have zero M_x and M_z components. Although there are three degrees of freedom of the magnetic moment on the Fe1 site, it aligns along the a direction with $M_x = -4.29$ μ_B and $M_y = M_z = 0$ μ_B in $RbFe_2F_6$. The Fe2 site acquires magnetization along the only symmetry allowed direction, the b direction, with $M_y = 3.99$ μ_B, resulting in an orthogonal arrangement of the magnetic moments on the two different metal sublattices. In contrast to the Fe analogs, $CsMn_2F_6$ exhibits a magnetic structure with *Pnm'a'* (#62.447) symmetry, for which the net magnetization of the unit cell can be nonzero along the a axis. The Mn1 site orders predominately along the b direction, $M_x = 0.05(10)$, $M_y = -3.234(14)$, $M_z = 0.36(6)$ μ_B, while the Mn2 site magnetization is perpendicular to the b axis due to symmetry constraints, $M_x = 0.16(8)$, $M_z = 0.57(4)$ μ_B. Given that the Mn2 site does not exhibit its full magnetic moment and stays in a mixed ordered/paramagnetic state, one can surmise that there is exchange between Mn1 and Mn2 site that prevents the latter from complete ordering. As temperature decreases and the symmetry of $CsMn_2F_6$ reduces to $P2_1/c$, the symmetry constraint on the Mn2 M_y component lifts, and it readily acquires magnetization along the b axis, resulting in an overall nearly parallel alignment of the magnetic moments, in stark contrast to orthogonal moments in $RbeFe_2F_6$. To better understand such magnetic structure transitions in $CsMn_2F_6$, we performed Density Functional Theory (DFT) calculations to shed light on exchange interactions occurring in this compound.

Theoretical Calculations of Magnetic Exchange Interactions in $CsMn_2F_6$. To clarify the complex magnetic behavior of $CsMn_2F_6$, we conducted first-principles DFT calculations. Five different collinear magnetic structures were selected for calculations: a ferromagnetic case (FM); a ferrimagnetic structure where different magnetic moments on the Mn1 and Mn2 sites orient antiparallel (FI1); a state with each of these 4-fold sites further subdivided into two antialigned 2-fold sites (FI2); and two antiferromagnetic states−the groundstate AF1, which most closely resembles the experimental magnetic structure, and AF2, which corresponds to the first excited state (Figure 11).

The results of DFT calculations are summarized in Table 1 and agree very well with the experimental observations. Despite significantly varying energies of the four most energetically favorble optimized structures, up to 59 meV/Mn atom, the magnetic moments on the Mn sites are consistent across the different structure, falling in the narrow ranges of 3.47−3.53 μ_B and 4.22−4.23 μ_B for Mn1 and Mn2, respectively, indicating their local character. The groundstate structure AF1 confirms charge ordering in $CsMn^{2+}Mn^{3+}F_6$

https://doi.org/10.1021/jacs.1c04245
J. Am. Chem. Soc. 2021, 143, 11554−11567

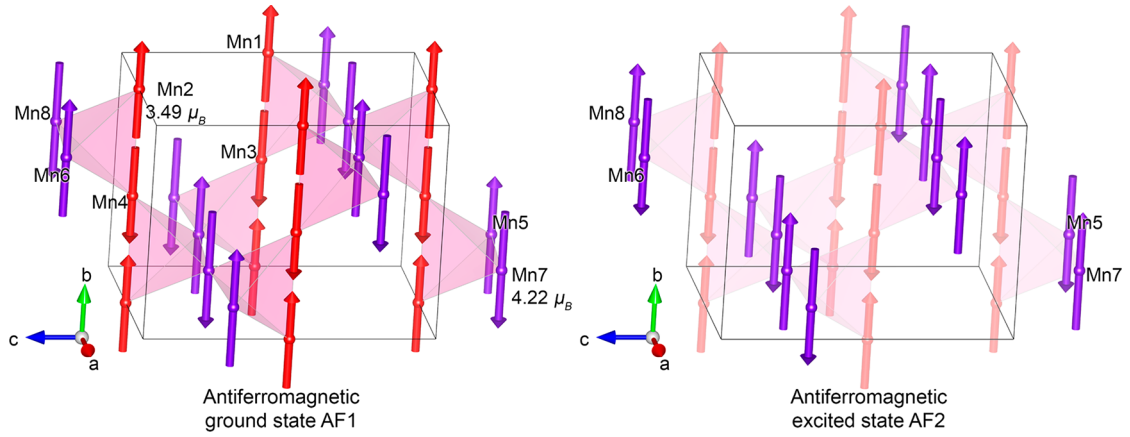

Figure 11. A depiction of the calculated AF1 groundstate. Atoms labeled Mn1 and Mn2 have a spin moment of 3.49 μ_B, Atoms Mn3 and Mn4 have −3.49 μ_B, while atoms Mn5 and Mn6 have 4.22 μ_B spin moment and Mn7 and Mn8 have −4.22 μ_B spin moment. In the first excited state, AF2Mn5 and Mn6 have −4.22 μ_B moment and Mn7 and Mn8 have 4.22 μ_B spin moment, with the other moments unchanged. Atoms Mn1−4 occupy the crystallographic Mn1 site and atoms Mn5−8 the crystallographic Mn2 site.

Table 1. DFT-Calculated Energies of Magnetic Structures and Magnetic Moments on the Mn Sites[a]

State	Energy above AF1 (meV/Mn)	Mn1 moment (μ_B)	Mn2 moment (μ_B)	Total moment (μ_B/f.u.)
FM	44.2	3.53	4.22	9.00
FI1	58.9	3.47	−4.23	−1.00
FI2	304.3	+3.50/−1.75	±4.22	+1.00
AF1	0	±3.49	±4.22	0
AF2	29.6	±3.49	±4.22	0

[a]Positive and negative magnetic moments are parallel and antiparallel to the b axis, respectively.

structure and is in excellent agreement with the experimental values obtained in the neutron diffraction experiment, 3.49 μ_B vs 3.40(3) and 3.52(4) μ_B for Mn1 sites and 4.22 μ_B vs 4.13(3) μ_B for Mn2 site. A good match between the calculated and experimental values indicates high accuracy of the selected calculation approach.

Previous reports show that the energy difference and first excited state may serve to probe the transition temperature as it depends on energies of competing states and can be calculated as three times the energy difference.[59−61] Applying this approach to $CsMn_2F_6$, one can expect a transition temperature at around 100 K, which is around four times higher than the temperature of the first transition. Such discrepancy highlights the significance on the spin non-collinearity as well as the presence of two phase transitions. Interestingly, both ground AF1 and first excited AF2 states have the same arrangements of the moments on the Mn1 site, which order magnetically first and therefore can be compared to the next excited state, FM. The energy difference between AF2 and FM levels, 14.6 eV/Mn atom, indicates a phase transition at 44 K, which is closer to the experimental value of 25 K, but deviates from it due to noncollinearity of the magnetic moments.

Calculations of the spin-density in the observed magnetic ground state (Figure S25) find a significant spatial extent of the Mn-based orbitals, with significant spin density associated with the F atoms, consistent with their exhibition of a slight (as high as 0.026 μ_B) spin moment in the calculations. This is an induced moment and derives from the relatively close distances of F to the Mn atoms (as close as 1.86 Å).

Finally, we comment briefly on the experimental finding of substantial hard magnetic behavior at the lowest temperatures, with coercive fields exceeding 5 T. Our main point here is that unlike in the case of ferromagnetic permanent magnet materials,[62−64] small net magnetizations M_s generated by canted antiferromagnets allow the generation of quite substantial anisotropy fields H_A and hence coercivities H_c, even if the effective first anisotropy constant K_1 is rather small. The reason is the inverse relationship between these quantities, which can be expressed in the equation $H_A = 2K_1/M_s$.[65] Quantitatively, if M_s is 0.008 μ_B per Mn, as in Figure 8, M_s is approximately 0.015 T, and for a K_1 assumed to be just 0.1 MJ/m^3 (nearly an order of magnitude smaller than in hcp cobalt, for example), one can expect an anisotropy field of nearly 17 T, which could well allow a coercivity as high as 5 T. This suggests that canted antiferromagnets, even whose magnetic elements are only the usually magnetically soft 3d elements, can produce highly coercive behavior which is of potential interest for spintronic and other applications.

CONCLUSIONS

We obtained a new charge ordered defect pyrochlore fluoride $CsMn^{2+}Mn^{3+}F_6$ *via* a hydrothermal route using CsCl to partially reduce Mn_2O_3 oxide in the presence of hydrofluoric acid. Crystallochemical analysis of the new and reported fluoride defect pyrochlore structures showed that their formation is promoted by smaller *M* site cations. Moreover, the present structural and synthetic data indicate that the formation of the ordered orthorhombic defect pyrochlore structure is favored by a large size difference between the M^{2+} and M^{3+} cations, small A cation sizes, and a moderate, ca. 300−500 °C temperature regimes during crystallization.

Magnetic susceptibility data collected using a powder sample of the new phase $CsMn_2F_6$ exhibits a transition to a long-range spin ordered state at 24 K, which was confirmed by neutron diffraction data that also revealed a second transition between 10 and 14 K. The first transition to the *Pnm'a'* magnetic space group is caused by spin ordering on the Mn^{3+} sublattice and partial ordering on the Mn^{2+} sublattice, while a complete ordering of the latter results in further symmetry lowering to the $P2_1/c$ magnetic space group during the second transition.

https://doi.org/10.1021/jacs.1c04245
J. Am. Chem. Soc. 2021, 143, 11554−11567

The canted antiferromagnetic ordering resulted in a 0.69 μ_B net magnetization in the unit cell along the *a* axis, which is consistent with a hysteresis loop and weak remnant magnetization observed in *M* vs *H* plots. Using DFT calculations, we found two low energy antiferromagnetic states, which differ by spin arrangement on the Mn^{2+} sites. The ground state structure matches the experimentally observed spin arrangement and the excited state is 29.6 meV/Mn atom above the groundstate. Given the discrepancy between predicted and experimental values of transition temperatures (100 vs 24.1 K, respectively), we conclude that canting is crucial for $CsMn_2F_6$ magnetic structure.

A notable feature of this material is that the coercive field of its ferromagnetic component is highly dependent on temperature and changes from nearly $H_c \approx 0$ T at around the transition temperature $T_{c,1}$ = 24.1 K to $H_c > 5$ T below 10 K. Such an effect results in an interesting phenomenon, in which the residual field in the SQUID instrument is sufficient to induce magnetization in the $CsMn_2F_6$ sample upon zero-field cooling, which then becomes an extremely hard magnet at 2 K, and the magnetization of the sample stays unaffected upon exposure to a 5 T field. Such an effect can be useful in a situation when there is a need to record data in a weak field and then to protect the data from fields that are orders of magnitude stronger than the recording field. Surprisingly, such behavior contrasts with purely antiferromagnetic AFe_2F_6 analogs, suggesting that the distortion of the M^{2+} site plays an important role in the properties of charge ordered defect pyrochlore fluorides $AM^{2+}M^{3+}F_6$.

EXPERIMENTAL SECTION

Caution! *Hydrofluoric acid is toxic and corrosive and must be handled with extreme caution and the appropriate protective gear! If contact with the liquid or vapor occurs, proper treatment procedures should immediately be followed.*

Caution! *Chlorine gas is released during the reactions described below. Chlorine gas causes acute damage in the upper and lower respiratory tract and must be handled in a well-ventilated hood with appropriate protective gear.*

General Considerations. All reagents were obtained from commercial sources and were used without further purification. Phase purity was confirmed by powder X-ray diffraction using a Bruker D2 Phaser instrument (Cu Kα, λ = 1.54184 Å).

Synthesis. A phase pure (by PXRD) powder of $CsMn_2F_6$ was obtained hydrothermally by reacting 0.70 g of Mn_2O_3 and 1.50 g of CsCl in a 1:2 molar ratio with 3.00 mL of 49% HF. The starting materials were mixed in a PTFE liner and sealed in a steel autoclave. The autoclave was heated to 200 °C for 12 h in a convection oven and cooled to room temperature by turning off the oven. After finishing the reaction, the autoclave was opened, releasing greenish, chlorine smelling gas. The product was filtered on a paper filter using a Buchner funnel and washed on the filter with about 50 mL of acetone. $CsMn_2F_6$ is stable in air for several months, but rapidly dissolves in water.

Large (0.1−0.5 mm^3) dark brown single crystals of $CsMn_2F_6$ along with a pale pink MnF_2 side product were obtained by reacting 0.350 g of Mn_2O_3, 0.56 g CsCl, and 0.17 g of CsF with 4.00 mL of 49% HF and 2.67 mL of H_2O. The reagents were sealed in a PTFE-lined steel autoclave and heated to 200 °C at a rate of 0.1 °C/min, made to dwell at this temperature for 12 h, and cooled to room temperature by shutting off the convection oven. We found that the crystal size is very sensitive to the PTFE liner that was used, with generally larger crystal size for the liners with a coarse surface, which presumably promotes nucleation sites for the product. Quantitative elemental analysis was performed on product single crystals using a Tescan Vega-3 SEM instrument equipped with a Thermo EDS attachment (Table S6 and Figure S26).

Phase pure (by PXRD) powder of $CsMnF_4$ was obtained by dehydrating a mixture of $CsMnF_4$ and $CsMnF_4{\cdot}2H_2O$ under a N_2 flow at 120 °C, well above the decomposition temperature of $CsMnF_4{\cdot}2H_2O$, 69−70 °C, which was determined using thermal gravimetric analysis (TGA) (Figures S27 and S28). The purity of $CsMnF_4$ was confirmed by PXRD (Figure S28). The mixture of $CsMnF_4$ and $CsMnF_4{\cdot}2H_2O$ was obtained by reacting 0.70 g of Mn_2O_3 and 1.35 g of CsF in a 1:2 molar ratio with 3.00 mL of 49% HF. The starting materials were mixed in a PTFE liner and sealed in a steel autoclave. The autoclave was heated to 200 °C for 12 h in a convection oven and cooled to room temperature by turning off the oven. The product was filtered on a paper filter using a Buchner funnel and washed on the filter with about 50 mL of acetone.

Crystal Structure. Single-crystal X-ray diffraction data were collected at 300(2) K on a Bruker D8 QUEST diffractometer equipped with an Incoatec IμS 3.0 microfocus radiation source (Mo Kα, λ = 0.71073 Å) and a PHOTON II area detector. The crystals were mounted on a microloop using immersion oil. The raw data reduction and absorption corrections were performed using SAINT and SADABS programs.[66,67] Initial structure solutions were obtained with SHELXS-2017 using direct methods and Olex2 GUI.[68] Full-matrix least-squares refinements against F^2 were performed with SHELXL software.[69] The crystallographic data and results of the diffraction experiments are summarized in Tables S2 and S3. Crystal data for $CsMn_2F_6$: space group *Pnma* (no. 62), *a* = 7.3013(2) Å, *b* = 7.7141(2) Å, *c* = 10.1926(3) Å, *V* = 574.08(3) $Å^3$, *Z* = 4, *T* = 301.46 K, μ(MoKα) = 10.681 mm^{-1}, D_{calc} = 4.128 g/cm^3, 6789 reflections measured (6.624° ≤ 2θ ≤ 54.966°), 708 unique (R_{int} = 0.0313, R_{sigma} = 0.0146) which were used in all calculations. The final R_1 was 0.0142 (I > 2σ(I)) and wR_2 was 0.0289 (all data).

Magnetism. Magnetic property measurements were performed using a Quantum Design MPMS 3 SQUID magnetometer. For DC measurements, 32.71 mg of thoroughly ground sample was sealed in a plastic VSM powder sample holder and placed in a brass sample holder. For single crystal DC measurements (Figure S4), a multidomain nonmerohedrally twinned crystal of about 1 × 1 × 0.2 mm^3 size was glued to a quartz paddle in a random orientation. AC measurements were carried out using 57.27 mg of powder sample sealed in a gelatin capsule. The zero-field cooled and field cooled measurements were carried out in the SQUID DC mode in the 2−300 K temperature range and in an applied field of 0.1 T. AC measurements for magnetic transition detection were performed at applied field H_{DC} = 0 and h_{ac} = 5 Oe with a frequency *f* of 5, 7.57, 15, 50, 100, 150, and 500 Hz. MvH plots were measured at applied field from −5 to 5 T at temperatures of 2, 5, 10, 15, 17.5, 20, 23.5, 24.5, and 25 K. Before collecting MvH data, the sample was heated to 300 K, and dwelled at this temperature for 10 min to ensure removal of remnant magnetization. For magnetic moment calculation, the DC magnetic susceptibility was corrected for sample shape and radial offset.[70]

To calculate the magnetic moment of $CsMn_2F_6$, several magnetic susceptibility vs temperature data sets from different reaction batches were collected, yielding consistent results with a magnetic moment of around 8.0 μ_B, which is higher than the theoretical value of 7.68 μ_B that was calculated based on spin only moments of 5.92 and 4.90 μ_B for Mn^{2+} and Mn^{3+}. For comparison, the magnetic susceptibility data for anhydrous $CsMnF_4$ were collected, resulting in the moment of 4.96 μ_B (Figure S29), which is consistent with the theoretical value of 4.90 μ_B for Mn^{3+}. The latter result precludes an instrumental error, while reproducibility of the results and the phase purity of the studied material based on PXRD and neutron diffraction, indicates that the higher than expected magnetic moment of $CsMn_2F_6$ is likely an intrinsic property of the material.

Neutron Diffraction. Neutron powder diffraction measurements were conducted at Oak Ridge National Laboratory (ORNL). Preliminary data at 40 and 10 K were obtained using the POWGEN automatic sample changer *via* the mail-in program of the POWGEN diffractometer at the Spallation Neutron Source (SNS) (Figure S6),

https://doi.org/10.1021/jacs.1c04245
J. Am. Chem. Soc. 2021, 143, 11554−11567

and temperature-dependent neutron diffraction data were collected on the instrument HB-2A at the High Flux Isotope Reactor (HFIR). For the experiment at HB-2A, a constant wavelength of 2.4067 Å was selected from the (113) reflection of a Ge monochromator. A PG filter was used to remove any scattering from higher order reflections. The sample was loaded in to a vanadium can and neutron diffraction data were collected at 1.5, 6, 10, 14−24 (with a 1 K step), 26, 40, and 290 K, well above the transition temperature (Figures S7−S24). The sample temperature was obtained using a top-loading ^{4}He cryostat with a 3-sample changer stick. No apparent impurities were detected in the neutron data. The data were collected using 44 ^{3}He detectors, with 12' collimation before each detector, in a Debye−Scherrer geometry that covered a 2θ range of 5−130 degrees. Data were collected in 0.05 degree steps. Figures S7−24 show neutron powder diffraction data along with the Rietveld refinements.

The magnetic structures were solved and refined using the Bilbao Crystallographic Server and FullProf Rietveld refinement suite.[71,72] The nuclear structure and refinement variables were refined against the diffraction data at 26 K, and the model was used to solve the magnetic structure at 18 K. The propagation vector **k** for the magnetic structure was found to be (0,0,0) by searching additional peaks in the difference diffraction pattern. The crystal structure of $CsMn_2F_6$ along with the propagation vector were uploaded to the MAGNEXT program on the Bilbao server and several possible magnetic space groups were found.[73,74] We found the best fitting magnetic structure in the *Pnm'a'* group by attempting trial structure refinements in different possible magnetic space groups. The obtained magnetic model was then refined against the other data sets at the temperatures between 24 and 10 K. Refinement of the same *Pnm'a'* model against the 1.5 K data revealed large residual peaks, indicating the presence of a second magnetic transition at lower temperatures. The symmetry of the low temperature magnetic phase was determined by removing symmetry elements from the *Pnm'a'* supergroup using MAGNEXT and refining the model against the 1.5 K data. The only reasonable solution was obtained using the $P2_1/n11$ space group, resulting in a good model with reasonable magnetic moments on the Mn atoms. The original cell can be transformed to the standard $P2_1/c$ setting by the (0 0−1 1 0 0 0−1 1) transformation matrix. The magnetic model was used for refinement against the 6 K data.

First-principle calculations were carried out using the all-electron code WIEN2K,[75,76] working within the generalized gradient approximation (GGA)[77] as well as calculations using its extension, the GGA+U approach, in which an additional potential is applied to the relevant atomic orbitals. All calculations were performed using the experimental structure as a starting model. Ordinarily, our approach is to employ the experimental lattice parameters and then relax nonsymmetry-dictated internal coordinates within an assumed ferromagnetic configuration, to account for potential magnetoelastic effects.[78−80] However, this procedure produced a structure far from the experimental one, including in particular Mn1−F distances as much as 0.1 Å larger than experiment, and in addition, tended to equalize the moments on the two Mn sites, again in contradiction to the experimental data. Structures optimized within antiferromagnetic arrangements yielded only slight structural improvement. This departure of optimized structures from experimental ones is reminiscent of the situation with the iron-based superconductors,[81] where relaxing the As height can yield a structure far from experiment. Here, the physics is of large Mn local moments coupling strongly to the lattice, and it is likely that the noncollinearity (not studied here) plays a significant role in the structure. For this reason, all calculations were performed in the experimental structure. Muffin-tin radii of 1.59, 1.76, and 2.50 Bohr were used, respectively, for the F, Mn, and Cs spheres, and an RK_{max} value (the product of the smallest radius and the largest plane-wave vector) of 7.0 was used; spin−orbit coupling was not employed. We report here results from the GGA+U approach with a U value of 5.25 eV applied to the Mn d orbitals.[82] Given the highly electronegative nature of fluorine, a correlated approach is likely more accurate than the straight GGA and, in fact, yields moment magnitudes in better agreement with the neutron results.

■ ASSOCIATED CONTENT

Supporting Information

The Supporting Information is available free of charge at https://pubs.acs.org/doi/10.1021/jacs.1c04245.

Crystallographic data, magnetic moments, a list of tolerance factors for $AM^{2+}M^{3+}F_6$ and $AAM_2{}^{+2}F_7$ compounds, DTA and TGA results, high temperature PXRD, neutron diffraction data and fitting, EDS results (PDF)

Accession Codes

CCDC 2079680 contain the supplementary crystallographic data for this paper. These data can be obtained free of charge via www.ccdc.cam.ac.uk/data_request/cif, or by emailing data_request@ccdc.cam.ac.uk, or by contacting The Cambridge Crystallographic Data Centre, 12 Union Road, Cambridge CB2 1EZ, UK; fax: + 44 1223 336033.

■ AUTHOR INFORMATION

Corresponding Author

Hans-Conrad zur Loye − *Department of Chemistry and Biochemistry, University of South Carolina, Columbia, South Carolina 29208, United States*; Email: zurloye@mailbox.sc.edu

Authors

Vladislav V. Klepov − *Department of Chemistry and Biochemistry, University of South Carolina, Columbia, South Carolina 29208, United States;* Present Address: currently at Department of Chemistry, Northwestern University, Evanston, Illinois, 60208, United States; orcid.org/0000-0002-2039-2457

Kristen A. Pace − *Department of Chemistry and Biochemistry, University of South Carolina, Columbia, South Carolina 29208, United States;* Present Address: currently at Pit Technologies Division, Los Alamos National Laboratory, Los Alamos, NM 87545, United States; orcid.org/0000-0001-8574-8939

Anna A. Berseneva − *Department of Chemistry and Biochemistry, University of South Carolina, Columbia, South Carolina 29208, United States*

Justin B. Felder − *Chemical Sciences Division, Oak Ridge National Laboratory, Oak Ridge, Tennessee 37831, United States;* orcid.org/0000-0002-2528-1967

Stuart Calder − *Neutron Scattering Division, Oak Ridge National Laboratory, Oak Ridge, Tennessee 37831, United States*

Gregory Morrison − *Department of Chemistry and Biochemistry, University of South Carolina, Columbia, South Carolina 29208, United States;* orcid.org/0000-0001-9674-9224

Qiang Zhang − *Neutron Scattering Division, Oak Ridge National Laboratory, Oak Ridge, Tennessee 37831, United States*

Melanie J. Kirkham − *Neutron Scattering Division, Oak Ridge National Laboratory, Oak Ridge, Tennessee 37831, United States;* orcid.org/0000-0001-8411-9751

David S. Parker − *Materials Science and Technology Division, Oak Ridge National Laboratory, Oak Ridge, Tennessee 37831, United States*

Complete contact information is available at: https://pubs.acs.org/10.1021/jacs.1c04245

Notes

The authors declare no competing financial interest.

■ ACKNOWLEDGMENTS

Financial support for this work was provided by the National Science Foundation under award DMR-1806279 and is gratefully acknowledged. This research used resources at the High Flux Isotope Reactor and the Spallation Neutron Source, a DOE Office of Science User Facility operated by the Oak Ridge National Laboratory. D.S.P (first-principles calculations) was supported by the U.S. Department of Energy, Office of Science, Basic Energy Sciences, Materials Science and Engineering Division.

■ REFERENCES

(1) Subramanian, M. A.; Toby, B. H.; Ramirez, A. P.; Marshall, W. J.; Sleight, A. W.; Kwei, G. H. Colossal Magnetoresistance Without Mn^{3+}/Mn^{4+} Double Exchange in the Stoichiometric Pyrochlore $Tl_2Mn_2O_7$. *Science* **1996**, *273* (5271), 81−84.

(2) Booth, C. H.; Gardner, J. S.; Kwei, G. H.; Heffner, R. H.; Bridges, F.; Subramanian, M. A. Local Lattice Disorder in the Geometrically Frustrated Spin-Glass Pyrochlore $Y_2Mo_2O_7$. *Phys. Rev. B: Condens. Matter Mater. Phys.* **2000**, *62* (2), R755−R758.

(3) Gardner, J. S.; Gingras, M. J. P.; Greedan, J. E. Magnetic Pyrochlore Oxides. *Rev. Mod. Phys.* **2010**, *82* (1), 53−107.

(4) Egorysheva, A. V.; Ellert, O. G.; Gaitko, O. M.; Berseneva, A. A.; Maksimov, Yu. V.; Dudkina, T. D. Magnetic Properties of $Pr_{2-x}Fe_{1+x}SbO_7$ and $Bi_{2-x}Ln_xFeSbO_7$ (Ln = La, Pr) Pyrochlore Solid Solutions. *Inorg. Mater.* **2016**, *52* (10), 1035−1044.

(5) Converse, E. S.; Li, J.; Haskel, D.; LaBarre, P. G.; Ramirez, A. P.; Subramanian, M. A. Os^{4+} Instability in the Pyrochlore Structure: $Tl_{2-x}Bi_xOs_2O_{7-y}$. *Inorg. Chem.* **2020**, *59* (2), 1227−1233.

(6) Sardar, K.; Petrucco, E.; Hiley, C. I.; Sharman, J. D. B.; Wells, P. P.; Russell, A. E.; Kashtiban, R. J.; Sloan, J.; Walton, R. I. Water-Splitting Electrocatalysis in Acid Conditions Using Ruthenate-Iridate Pyrochlores. *Angew. Chem., Int. Ed.* **2014**, *53* (41), 10960−10964.

(7) Urban, S.; Djerdj, I.; Dolcet, P.; Chen, L.; Möller, M.; Khalid, O.; Camuka, H.; Ellinghaus, R.; Li, C.; Gross, S.; Klar, P. J.; Bernd Smarsly Over, H. In Situ Study of the Oxygen-Induced Transformation of Pyrochlore $Ce_2Zr_2O_{7+x}$ to the κ-$Ce_2Zr_2O_8$ Phase. *Chem. Mater.* **2017**, *29* (21), 9218−9226.

(8) Kuznetsov, D. A.; Naeem, M. A.; Kumar, P. V.; Abdala, P. M.; Fedorov, A.; Müller, C. R. Tailoring Lattice Oxygen Binding in Ruthenium Pyrochlores to Enhance Oxygen Evolution Activity. *J. Am. Chem. Soc.* **2020**, *142* (17), 7883−7888.

(9) Li, C.; Yin, C.; Gu, L.; Dinnebier, R. E.; Mu, X.; van Aken, P. A.; Maier, J. An $FeF_3{\cdot}0.5H_2O$ Polytype: A Microporous Framework Compound with Intersecting Tunnels for Li and Na Batteries. *J. Am. Chem. Soc.* **2013**, *135* (31), 11425−11428.

(10) Xu, J.; Wang, D.; Kong, S.; Li, R.; Hong, Z.; Huang, F. Pyrochlore Phase $Ce_2Sn_2O_7$*via* an Atom-Confining Strategy for Reversible Lithium Storage. *J. Mater. Chem. A* **2020**, *8* (11), 5744−5749.

(11) Nyman, M.; Rodriguez, M. A.; Shea-Rohwer, L. E.; Martin, J. E.; Provencio, P. P. Highly Versatile Rare Earth Tantalate Pyrochlore Nanophosphors. *J. Am. Chem. Soc.* **2009**, *131* (33), 11652−11653.

(12) Laurita, G.; Hickox-Young, D.; Husremovic, S.; Li, J.; Sleight, A. W.; Macaluso, R.; Rondinelli, J. M.; Subramanian, M. A. Covalency-Driven Structural Evolution in the Polar Pyrochlore Series $Cd_2Nb_2O_{7-x}S_x$. *Chem. Mater.* **2019**, *31* (18), 7626−7637.

(13) Subramanian, M. A.; Aravamudan, G.; Subba Rao, G. V. Oxide Pyrochlores — A Review. *Prog. Solid State Chem.* **1983**, *15* (2), 55−143.

(14) Greedan, J. E. Frustrated Rare Earth Magnetism: Spin Glasses, Spin Liquids and Spin Ices in Pyrochlore Oxides. *J. Alloys Compd.* **2006**, *408*−*412*, 444−455.

(15) Sanders, M. B.; Krizan, J. W.; Cava, R. J. $RE_3Sb_3Zn_2O_{14}$ (RE = La, Pr, Nd, Sm, Eu, Gd): A New Family of Pyrochlore Derivatives with Rare Earth Ions on a 2D Kagome Lattice. *J. Mater. Chem. C* **2016**, *4* (3), 541−550.

(16) Silverstein, H. J.; Fritsch, K.; Flicker, F.; Hallas, A. M.; Gardner, J. S.; Qiu, Y.; Ehlers, G.; Savici, A. T.; Yamani, Z.; Ross, K. A.; Gaulin, B. D.; Gingras, M. J. P.; Paddison, J. A. M.; Foyevtsova, K.; Valenti, R.; Hawthorne, F.; Wiebe, C. R.; Zhou, H. D. Liquidlike Correlations in Single-Crystalline $Y_2Mo_2O_7$: An Unconventional Spin Glass. *Phys. Rev. B: Condens. Matter Mater. Phys.* **2014**, *89* (5), 054433.

(17) Snyder, J.; Ueland, B. G.; Slusky, J. S.; Karunadasa, H.; Cava, R. J.; Schiffer, P. Low-Temperature Spin Freezing in the $Dy_2Ti_2O_7$ Spin Ice. *Phys. Rev. B: Condens. Matter Mater. Phys.* **2004**, *69* (6), 064414.

(18) Fennell, T.; Deen, P. P.; Wildes, A. R.; Schmalzl, K.; Prabhakaran, D.; Boothroyd, A. T.; Aldus, R. J.; McMorrow, D. F.; Bramwell, S. T. Magnetic Coulomb Phase in the Spin Ice $Ho_2Ti_2O_7$. *Science* **2009**, *326* (5951), 415−417.

(19) Sibille, R.; Lhotel, E.; Ciomaga Hatnean, M.; Nilsen, G. J.; Ehlers, G.; Cervellino, A.; Ressouche, E.; Frontzek, M.; Zaharko, O.; Pomjakushin, V.; Stuhr, U.; Walker, H. C.; Adroja, D. T.; Luetkens, H.; Baines, C.; Amato, A.; Balakrishnan, G.; Fennell, T.; Kenzelmann, M. Coulomb Spin Liquid in Anion-Disordered Pyrochlore $Tb_2Hf_2O_7$. *Nat. Commun.* **2017**, *8* (1), 892.

(20) Xu, J.; Benton, O.; Islam, A. T. M. N.; Guidi, T.; Ehlers, G.; Lake, B. Order out of a Coulomb Phase and Higgs Transition: Frustrated Transverse Interactions of $Nd_2Zr_2O_7$. *Phys. Rev. Lett.* **2020**, *124* (9), 097203.

(21) Krizan, J. W.; Cava, R. J. $NaCaNi_2F_7$: A Frustrated High-Temperature Pyrochlore Antiferromagnet with S = 1 Ni^{2+}. *Phys. Rev. B: Condens. Matter Mater. Phys.* **2015**, *92* (1), 014406.

(22) Krizan, J. W.; Cava, R. J. $NaSrCo_2F_7$, a Co^{2+} Pyrochlore Antiferromagnet. *J. Phys.: Condens. Matter* **2015**, *27* (29), 296002.

(23) Ross, K. A.; Brown, J. M.; Cava, R. J.; Krizan, J. W.; Nagler, S. E.; Rodriguez-Rivera, J. A.; Stone, M. B. Single-Ion Properties of the S_{Eff} = 1/2 XY Antiferromagnetic Pyrochlores NaA'Co_2F_7 (A′ = Ca^{2+}, Sr^{2+}). *Phys. Rev. B: Condens. Matter Mater. Phys.* **2017**, *95* (14), 144414.

(24) Sanders, M. B.; Krizan, J. W.; Plumb, K. W.; McQueen, T. M.; Cava, R. J. $NaSrMn_2F_7$, $NaCaFe_2F_7$, and $NaSrFe_2F_7$: Novel Single Crystal Pyrochlore Antiferromagnets. *J. Phys.: Condens. Matter* **2017**, *29* (4), 045801.

(25) Wanklyn, B. M.; Wondre, F. R.; Garrard, B. J.; Cermak, J.; Davison, W. Flux Growth of Crystals of Some Transition Metal Fluorides: Part 3 Pyrochlores and Others. *J. Mater. Sci.* **1981**, *16* (8), 2303−2309.

(26) Fedorov, P. P.; Alexandrov, A. A. Synthesis of Inorganic Fluorides in Molten Salt Fluxes and Ionic Liquid Mediums. *J. Fluorine Chem.* **2019**, *227*, 109374.

(27) Harris, M. J.; Zinkin, M. P.; Tun, Z.; Wanklyn, B. M.; Swainson, I. P. Magnetic Structure of the Spin-Liquid State in a Frustrated Pyrochlore. *Phys. Rev. Lett.* **1994**, *73* (1), 189−192.

(28) Harris, M. J.; Zinkin, M. P.; Zeiske, T. Magnetic Excitations in a Highly Frustrated Pyrochlore Antiferromagnet. *Phys. Rev. B: Condens. Matter Mater. Phys.* **1995**, *52* (2), R707−R710.

(29) Fennell, T.; Harris, M. J.; Calder, S.; Ruminy, M.; Boehm, M.; Steffens, P.; Lemée-Cailleau, M.-H.; Zaharko, O.; Cervellino, A.; Bramwell, S. T. Multiple Coulomb Phase in the Fluoride Pyrochlore $CsNiCrF_6$. *Nat. Phys.* **2019**, *15* (1), 60−66.

(30) Garrard, B. J.; Wanklyn, B. M. Flux Growth of Some Fluoride Crystals under Reducing Conditions. IV. *J. Cryst. Growth* **1979**, *47* (2), 159−163.

(31) Ferey, G.; Leblanc, M.; De Pape, R.; Pannetier, J. Frustrated Magnetic Structures: II. Antiferromagnetic Structure of the Ordered Modified Pyrochlore $NH_4Fe^{II}Fe^{III}F_6$ at 4.2 K. *Solid State Commun.* **1985**, *53* (6), 559−563.

(32) Raju, N. P.; Greedan, J. E.; Subramanian, M. A.; Adams, C. P.; Mason, T. E. Magnetic and Specific Heat Studies of the Cation-Ordered Pyrochlore NH_4CoAlF_6. *Phys. Rev. B: Condens. Matter Mater. Phys.* **1998**, *58* (9), 5550−5553.

(33) Kim, S. W.; Kim, S.-H.; Halasyamani, P. S.; Green, M. A.; Bhatti, K. P.; Leighton, C.; Das, H.; Fennie, C. J. $RbFe^{2+}Fe^{3+}F_6$: Synthesis, Structure, and Characterization of a New Charge-Ordered Magnetically Frustrated Pyrochlore-Related Mixed-Metal Fluoride. *Chem. Sci.* **2012**, *3* (3), 741−751.
(34) Molokeev, M. S.; Bogdanov, E. V.; Misyul, S. V.; Tressaud, A.; Flerov, I. N. Crystal Structure and Phase Transition Mechanisms in $CsFe_2F_6$. *J. Solid State Chem.* **2013**, *200*, 157−164.
(35) Ueda, H.; Yamada, K.; Yamauchi, H.; Ueda, Y.; Yoshimura, K. Electrical Conduction Mediated by Fluorine Atoms in the Pyrochlore Fluorides RbV_2F_6 and CsV_2F_6 with Mixed-Valent V Atoms. *Phys. Rev. B: Condens. Matter Mater. Phys.* **2016**, *93* (19), 195168.
(36) Fleischer, T.; Hoppe, R. Zur kenntnis der $RbNiCrF_6$-familie [1,2,3]: Neue fluoride $A^IM^{II}M^{III}F_6$ (AI = Cs,Rb; M^{II} = Mg,Ni,Cu,Zn; und M^{III} = Al,V,Fe,Co,Ni). *J. Fluorine Chem.* **1982**, *19* (3−6), 529−552.
(37) Hoppe, R.; Wingefeld, G. Zur Kenntnis des Systems Cs/Cu/F: Über $CsCu^{II}Cu^{III}F_6$. *Z. Anorg. Allg. Chem.* **1984**, *519* (12), 189−194.
(38) Goodenough, J. B. Jahn-Teller Phenomena in Solids. *Annu. Rev. Mater. Sci.* **1998**, *28*, 1−27.
(39) Subramanian, M. A.; Marshall, W. J.; Harlow, R. L. NH4CoAlF6: A Pyrochlore-Related Phase Existing in Both Ordered and Disordered Forms. *Mater. Res. Bull.* **1996**, *31* (6), 585−591.
(40) Songvilay, M.; Rodriguez, E. E.; Lindsay, R.; Green, M. A.; Walker, H. C.; Rodriguez-Rivera, J. A.; Stock, C. Anharmonic Magnon Excitations in Noncollinear and Charge-Ordered $RbFe^{2+}Fe^{3+}F_6$. *Phys. Rev. Lett.* **2018**, *121* (8), 087201.
(41) Yeon, J.; Smith, M. D.; Tapp, J.; Möller, A.; zur Loye, H.-C. Mild Hydrothermal Crystal Growth, Structure, and Magnetic Properties of Ternary U(IV) Containing Fluorides: $LiUF_5$, KU_2F_9, $K_7U_6F_{31}$, $RbUF_5$, RbU_2F_9, and RbU_3F_{13}. *Inorg. Chem.* **2014**, *53* (12), 6289−6298.
(42) Yeon, J.; Smith, M. D.; Tapp, J.; Möller, A.; zur Loye, H.-C. Application of a Mild Hydrothermal Approach Containing an in Situ Reduction Step to the Growth of Single Crystals of the Quaternary U(IV)-Containing Fluorides $Na_4MU_6F_{30}$ (M = Mn^{2+}, Co^{2+}, Ni^{2+}, Cu^{2+}, and Zn^{2+}) Crystal Growth, Structures, and Magnetic Properties. *J. Am. Chem. Soc.* **2014**, *136* (10), 3955−3963.
(43) Kim, S. W.; Zhang, R.; Halasyamani, P. S.; Hayward, M. A. $K_4Fe_3F_{12}$: An Fe^{2+}/Fe^{3+} Charge-Ordered, Ferrimagnetic Fluoride with a Cation-Deficient, Layered Perovskite Structure. *Inorg. Chem.* **2015**, *54* (13), 6647−6652.
(44) Gerke, B.; Tran, T. T.; Pöttgen, R.; Halasyamani, P. S. 119Sn Mössbauer Spectroscopy of Solvothermally Synthesized Fluorides $ASnF_3$ (A = Na, K, Rb, Cs). *Z. Naturforsch., B: J. Chem. Sci.* **2015**, *70* (10), 765−767.
(45) Tran, T. T.; He, J.; Rondinelli, J. M.; Halasyamani, P. S. $RbMgCO_3F$: A New Beryllium-Free Deep-Ultraviolet Nonlinear Optical Material. *J. Am. Chem. Soc.* **2015**, *137* (33), 10504−10507.
(46) Ayer, G. B.; Klepov, V. V.; Smith, M. D.; zur Loye, H.-C. Mild Hydrothermal Synthesis of the Complex Hafnium-Containing Fluorides $Cs_2[M(H_2O)_6][Hf_2F_{12}]$ (M = Ni, Co, Zn), $CuHfF_6(H_2O)_4$, and $Cs_2Hf_3Mn_3F_{20}$ Based on HfF_7 and HfF_6 Coordination Polyhedra. *Inorg. Chem.* **2019**, *58* (19), 13049−13057.
(47) Hancock, J. C.; Nisbet, M. L.; Zhang, W.; Halasyamani, P. S.; Poeppelmeier, K. R. Periodic Tendril Perversion and Helices in the $AMoO_2F_3$ (A = K, Rb, NH_4, Tl) Family. *J. Am. Chem. Soc.* **2020**, *142* (13), 6375−6380.
(48) Ayer, G. B.; Klepov, V. V.; Pace, K. A.; zur Loye, H.-C. Quaternary Cerium(IV) Containing Fluorides Exhibiting Ce_3F_{16} Sheets and Ce_6F_{30} Frameworks. *Dalton Trans.* **2020**, *49* (18), 5898−5905.
(49) Bukovec, P.; Kaučič, V. Synthesis and Crystal Structure of Caesium Diaquatetrafluoromanganate(III). *J. Chem. Soc., Dalton Trans.* **1977**, *9*, 945−947.
(50) Massa, W. Structural Chemistry and Jahn-Teller Effect in Fluoromanganates(III). *Rev. Inorg. Chem.* **1999**, *19* (1−2), 117−183.
(51) Song, Z.; Liu, Q. Tolerance Factor, Phase Stability and Order−Disorder of the Pyrochlore Structure. *Inorg. Chem. Front.* **2020**, *7* (7), 1583−1590.
(52) Shannon, R. Revised Effective Ionic Radii and Systematic Studies of Interatomic Distances in Halides and Chalcogenides. *Acta Crystallogr., Sect. A: Cryst. Phys., Diffr., Theor. Gen. Crystallogr.* **1976**, *32* (5), 751−767.
(53) Sidey, V. On the Effective Ionic Radii for Ammonium. *Acta Crystallogr., Sect. B: Struct. Sci., Cryst. Eng. Mater.* **2016**, *72* (4), 626−633.
(54) Lemoine, K.; Moury, R.; Durand, E.; Dompablo, E. A.; Morán, E.; Leblanc, M.; Hémon-Ribaud, A.; Grenèche, J.-M.; Galven, C.; Gunes, V.; Lhoste, J.; Maisonneuve, V. First Mixed-Metal Fluoride Pyrochlores Obtained by Topotactic Oxidation of Ammonium Fluorides under F_2 Gas. *Cryst. Growth Des.* **2021**, *21* (2), 935−945.
(55) Töpfer, J.; Goodenough, J. B. $LaMnO_{3+\delta}$Revisited. *J. Solid State Chem.* **1997**, *130* (1), 117−128.
(56) Pace, K. A.; Klepov, V. V.; Christian, M. S.; Morrison, G.; Deason, T. K.; Kutahyali Aslani, C.; Besmann, T. M.; Diprete, D. P.; Amoroso, J. W.; zur Loye, H.-C. Targeting Complex Plutonium Oxides by Combining Crystal Chemical Reasoning with Density-Functional Theory Calculations: The Quaternary Plutonium Oxide $Cs_2PuSi_6O_{15}$. *Chem. Commun.* **2020**, *56* (66), 9501−9504.
(57) Gorev, M. V.; Flerov, I. N.; Tressaud, A.; Bogdanov, E. V.; Kartashev, A. V.; Bayukov, O. A.; Eremin, E. V.; Krylov, A. S. Heat Capacity and Magnetic Properties of Fluoride $CsFe^{2+}Fe^{3+}F_6$ with Defect Pyrochlore Structure. *J. Solid State Chem.* **2016**, *237*, 330−335.
(58) Liu, S.; Xu, Y.; Cui, Y.; Wang, J.; Sun, K.; Yu, S.; Hao, X. Charge Ordering and Magnetic Frustration in $CsFe_2F_6$. *J. Phys.: Condens. Matter* **2017**, *29* (31), 315501.
(59) May, A. F.; Liu, Y.; Calder, S.; Parker, D. S.; Pandey, T.; Cakmak, E.; Cao, H.; Yan, J.; McGuire, M. A. Magnetic Order and Interactions in Ferrimagnetic Mn3Si2Te6. *Phys. Rev. B: Condens. Matter Mater. Phys.* **2017**, *95* (17), 174440.
(60) Lamichhane, T. N.; Taufour, V.; Masters, M. W.; Parker, D. S.; Kaluarachchi, U. S.; Thimmaiah, S.; Bud'ko, S. L.; Canfield, P. C. Discovery of Ferromagnetism with Large Magnetic Anisotropy in ZrMnP and HfMnP. *Appl. Phys. Lett.* **2016**, *109* (9), 092402.
(61) Pandey, T.; Du, M.-H.; Parker, D. S. Tuning the Magnetic Properties and Structural Stabilities of the 2−17−3 Magnets $Sm_2Fe_{17}X_3$ (X = C, N) by Substituting La or Ce for Sm. *Phys. Rev. Appl.* **2018**, *9* (3), 034002.
(62) McGuire, M. A.; Parker, D. S. Magnetic and Structural Properties of Ferromagnetic Fe_5PB_2 and Fe_5SiB_2 and Effects of Co and Mn Substitutions. *J. Appl. Phys.* **2015**, *118* (16), 163903.
(63) Williams, T. J.; Taylor, A. E.; Christianson, A. D.; Hahn, S. E.; Fishman, R. S.; Parker, D. S.; McGuire, M. A.; Sales, B. C.; Lumsden, M. D. Extended Magnetic Exchange Interactions in the High-Temperature Ferromagnet MnBi. *Appl. Phys. Lett.* **2016**, *108* (19), 192403.
(64) Lamichhane, T. N.; Xiang, L.; Lin, Q.; Pandey, T.; Parker, D. S.; Kim, T.-H.; Zhou, L.; Kramer, M. J.; Bud'ko, S. L.; Canfield, P. C. Magnetic Properties of Single Crystalline Itinerant Ferromagnet $AlFe_2B_2$. *Phys. Rev. Materials* **2018**, *2* (8), 084408.
(65) Yin, L.; Juneja, R.; Lindsay, L.; Pandey, T.; Parker, D. S. Semihard Iron-Based Permanent-Magnet Materials. *Phys. Rev. Appl.* **2021**, *15* (2), 024012.
(66) *SAINT*; Bruker AXS Inc.: Madison, Wisconsin, USA, 2012.
(67) Krause, L.; Herbst-Irmer, R.; Sheldrick, G. M.; Stalke, D. Comparison of Silver and Molybdenum Microfocus X-Ray Sources for Single-Crystal Structure Determination. *J. Appl. Crystallogr.* **2015**, *48* (1), 3−10.
(68) Dolomanov, O. V.; Bourhis, L. J.; Gildea, R. J.; Howard, J. A. K.; Puschmann, H. OLEX2: A Complete Structure Solution, Refinement and Analysis Program. *J. Appl. Crystallogr.* **2009**, *42* (2), 339−341.
(69) Sheldrick, G. M. Crystal Structure Refinement with *SHELXL*. *Acta Crystallogr., Sect. C: Struct. Chem.* **2015**, *71* (1), 3−8.

(70) Morrison, G.; zur Loye, H.-C. Simple Correction for the Sample Shape and Radial Offset Effects on SQUID Magnetometers: Magnetic Measurements on Ln_2O_3 (Ln = Gd, Dy, Er) Standards. *J. Solid State Chem.* **2015**, *221*, 334−337.
(71) Aroyo, M. I.; Perez-Mato, J. M.; Capillas, C.; Kroumova, E.; Ivantchev, S.; Madariaga, G.; Kirov, A.; Wondratschek, H. Bilbao Crystallographic Server: I. Databases and Crystallographic Computing Programs *Z. Kristallogr. - Cryst. Mater.* **2006**, *221* (1).15
(72) Aroyo, M. I.; Kirov, A.; Capillas, C.; Perez-Mato, J. M.; Wondratschek, H. Bilbao Crystallographic Server. II. Representations of Crystallographic Point Groups and Space Groups. *Acta Crystallogr., Sect. A: Found. Crystallogr.* **2006**, *62* (2), 115−128.
(73) Gallego, S. V.; Tasci, E. S.; de la Flor, G.; Perez-Mato, J. M.; Aroyo, M. I. Magnetic Symmetry in the Bilbao Crystallographic Server: A Computer Program to Provide Systematic Absences of Magnetic Neutron Diffraction. *J. Appl. Crystallogr.* **2012**, *45* (6), 1236−1247.
(74) Perez-Mato, J. M.; Gallego, S. V.; Tasci, E. S.; Elcoro, L.; de la Flor, G.; Aroyo, M. I. Symmetry-Based Computational Tools for Magnetic Crystallography. *Annu. Rev. Mater. Res.* **2015**, *45* (1), 217−248.
(75) Blaha, P.; Schwarz, K.; Madsen, G. K. H.; Kvasnicka, D.; Luitz, J.; Laskowsk, R.; Tran, F.; Marks, L.; Marks, L. *WIEN2k: An Augmented Plane Wave Plus Local Orbitals Program for Calculating Crystal Properties*; Techn. Universitat, 2019.
(76) Blaha, P.; Schwarz, K.; Tran, F.; Laskowski, R.; Madsen, G. K. H.; Marks, L. D. WIEN2k: An APW+lo Program for Calculating the Properties of Solids. *J. Chem. Phys.* **2020**, *152* (7), 074101.
(77) Perdew, J. P.; Burke, K.; Ernzerhof, M. Generalized Gradient Approximation Made Simple. *Phys. Rev. Lett.* **1996**, *77* (18), 3865−3868.
(78) Pokharel, G.; May, A. F.; Parker, D. S.; Calder, S.; Ehlers, G.; Huq, A.; Kimber, S. A. J.; Arachchige, H. S.; Poudel, L.; McGuire, M. A.; Mandrus, D.; Christianson, A. D. Negative Thermal Expansion and Magnetoelastic Coupling in the Breathing Pyrochlore Lattice Material $LiGaCr_4S_8$. *Phys. Rev. B: Condens. Matter Mater. Phys.* **2018**, *97* (13), 134117.
(79) Yan, J.-Q.; Liu, Y. H.; Parker, D. S.; Wu, Y.; Aczel, A. A.; Matsuda, M.; McGuire, M. A.; Sales, B. C. A-Type Antiferromagnetic Order in $MnBi_4Te_7$ and $MnBi_6Te_{10}$ Single Crystals. *Phys. Rev. Materials* **2020**, *4* (5), 054202.
(80) Sanjeewa, L. D.; Xing, J.; Taddei, K. M.; Parker, D.; Custelcean, R.; dela Cruz, C.; Sefat, A. S. Evidence of Ba-Substitution Induced Spin-Canting in the Magnetic Weyl Semimetal $EuCd_2As_2$. *Phys. Rev. B: Condens. Matter Mater. Phys.* **2020**, *102* (10), 104404.
(81) Mazin, I. I. Superconductivity Gets an Iron Boost. *Nature* **2010**, *464* (7286), 183−186.
(82) Floris, A.; de Gironcoli, S.; Gross, E. K. U.; Cococcioni, M. Vibrational Properties of MnO and NiO from DFT + U -Based Density Functional Perturbation Theory. *Phys. Rev. B: Condens. Matter Mater. Phys.* **2011**, *84* (16), 161102.

https://doi.org/10.1021/jacs.1c04245
J. Am. Chem. Soc. 2021, 143, 11554−11567